Recent thermokarst evolution in the Italian Central Alps

Mauro Guglielmin[1] | Stefano Ponti[1] | Emanuele Forte[2] | Nicoletta Cannone[3]

[1]Department of Theoretical and Applied Sciences, Insubria University, Varese, Italy

[2]Department of Mathematics and Geosciences, Trieste University, Trieste, Italy

[3]Department of Science and High Technology, Insubria University, Como, Italy

Abstract

Thermokarst depressions are widespread phenomena due to permafrost degradation in the Arctic, whereas only few are known from mountain permafrost of the mid-latitudes. In the Italian Central Alps, close to the Stelvio Pass (2,763 m above sea level), a ski run was built in 1987. Since 1981, statistically significant air warming has been recorded, especially during summer (+0.65°C per decade). Permafrost temperature recorded at the nearby Share Stelvio Borehole between 1990 and 2011 exhibited a rapid increase (> 0.8°C per decade) and an active-layer thickening (7 cm/year). Between the years 1999 and 2003, some thermokarst depressions started to develop, initially in the lower part of the ski run and then extending to higher elevations. The depressions increased in number, size, and depth with time. Since ski-run construction, the area remained free of vegetation until early 2000, when vegetation colonization started, showing a coupling with the onset of thermokarst development and summer warming. Vegetation changes accelerated with the ingress of pioneer and early-successional as well as of late-successional species. Moreover, the ingress of shrub species (*Salix* spp.) typical of lower elevation belts (subalpine and even montane) was dated to 2004. All the observed features show a rapid and coupled response of the abiotic and biotic components of this ecosystem to climate warming. Our data also confirm the similarity of the observed responses and dynamics of the alpine tundra with the Arctic tundra with regard to both permafrost and vegetation.

KEYWORDS

Alpine permafrost, anthropogenic effect, thermokarst, vegetation dynamics

1 | INTRODUCTION

The term "thermokarst" encompasses a wide range of thaw-related phenomena resulting from water on ice-rich permafrost landscapes.[1] Thermokarst landforms relate to the thawing of ice-rich permafrost or to the melting of massive ice[1–4] and include thermokarst lakes, basins, mounds, and alasses, but also active-layer detachments on slopes[5,6] and retrogressive thaw slumps (RTS).[1,7,8]

The different types of thermokarst landforms depend mainly on the source of heat (static or flowing water, or air), on ice type (ice wedges, segregated ice, intrusive ice, etc.), and indirectly on the characteristics of the deposit in which the ice occurs and on the relief morphology.[7] Thermokarst depressions are widespread features in the Arctic and have been inferred even on the planet Mars at the Utopia Planitia (e.g., [9]) but, to our knowledge, they have never been reported in mid-latitude alpine regions outside of rock glaciers. Indeed, the only thermokarst landforms reported in alpine environments are localized within rock glaciers and debris-covered glaciers in tropical high mountains (e.g., [10,11]) or relate to alpine thermokarst lakes.[12,13]

Climate warming in recent decades has induced widespread permafrost degradation and thermokarst activity, especially in the Arctic (e.g., [5,6,8,14,15]). Thermokarst activity has important impacts on hydrological processes (i.e.,[16,17]), terrestrial and freshwater ecosystems[18–20]), and infrastructure.[21,22] Several methods have been applied to estimate the susceptibility of landscapes to permafrost degradation and monitor its development with time (e.g.,[19,20,23,24]).

The case study presented here provides an important and novel insight into alpine thermokarst activity, making it fundamental to

understand the dynamics of the permafrost thermokarst formation without lakes. Indeed, the original landscape (and therefore the ground conditions) was completely reset by the anthropogenic action related to construction of a ski-run between 1987 and 1991. This involved the total destruction of a rock glacier and the partial obliteration of some solifluction lobes, allowing us to precisely determine the age of the new surface on which thermokarst activity has occurred subsequently, which can be established as 1991. No further construction activity, artificial snow production, or snow treatment has subsequently occurred.

The aims of this paper are: (a) to describe and quantify (at least in outline) the formation and the development of thermokarst landforms at the lower margin of permafrost distribution in a mid-latitude alpine environment; (b) to analyze the relationships among climate change, anthropogenic effects of the ski-run construction, and thermokarst development in the last 30 years; and (c) to analyze the effects of climate and permafrost changes on vegetation colonization and dynamics in the same anthropogenic areas.

2 | STUDY AREA

The study area is located in the Stelvio National Park (Italian central Alps), close to the Stelvio Pass (46°31′N, 10°25′E; elevation 2,230–3,095 m above sea level (asl); Figure 1). It includes the alpine (2,400–2,800 m asl) and nival belts (>2,800 m asl). The area is characterized by bedrock outcrops, as well as some Holocene till and talus deposits. The bedrock is mainly siliceous (consisting of granitic and granodioritic orthogneiss, schists, and biotite or two-mica paragneiss), with some localized outcrops of calcareous rock.[25,26]

In the area shown in Figure 1a, the slopes are mainly north-northwest exposed, with gradients ranging between 0.2° along the northern part of the ski run to a maximum of 42° on the southernmost part of the ski run, and an average of 17.8°. The study area does not show any thermokarst landform except for the thermokarst depressions reported and discussed in this paper. Several periglacial features occur, including solifluction lobes, scree slopes, block streams, and one active rock glacier,[25] although before the ski run construction a second rock glacier was present.

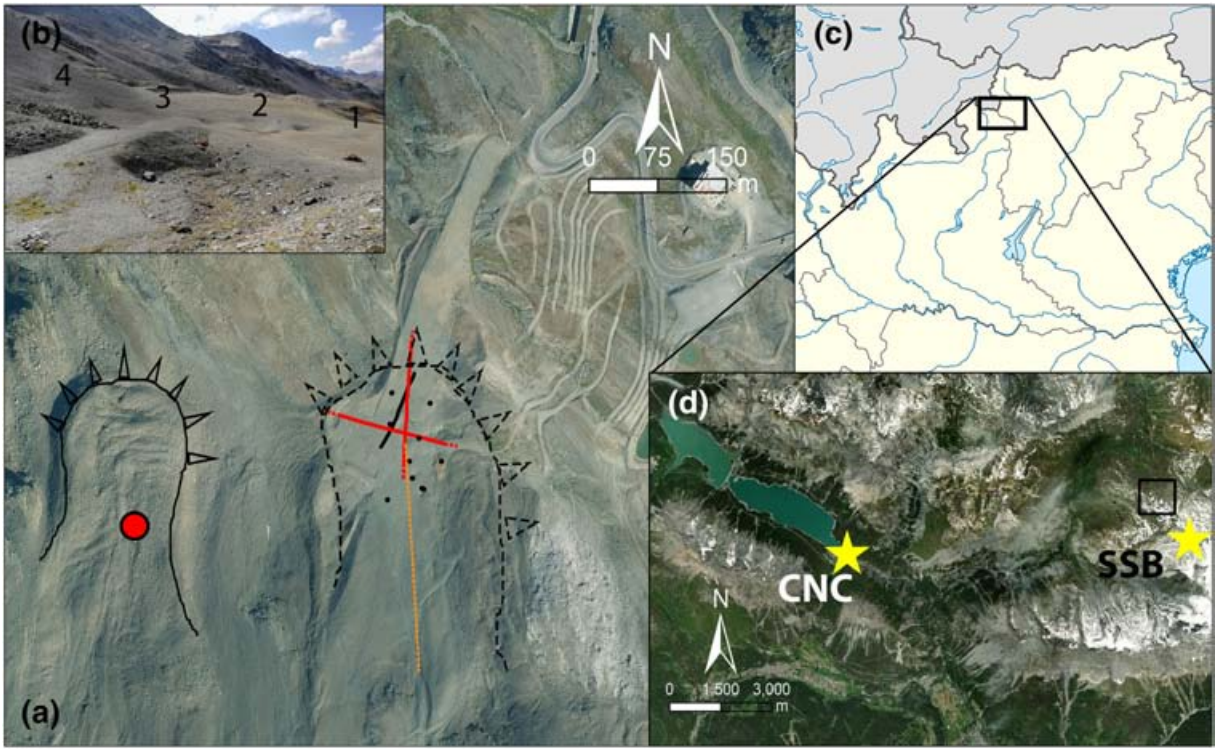

FIGURE 1 Study area details. (a) View of the ski run in the orthophoto of 2015 (https://www.geoportale.regione.lombardia.it/) with the location of geophysical investigations reported in the paper. GPR profile (black line) and ERT profiles (red lines: The older ERT reported in Figure 3a and Figure 4a and carried out respectively in 2014 and 2010 extended for all the lines including the dashed parts, whereas the others are located only along the solid lines), the ERT profile reported in Cannone et al.[28] carried out in 1998 (orange line), and vertical electric soundings (VES, carried out in 1993, red dot); the active rock glacier still present is underlined by the black solid line with triangles while the location of the rock glacier destroyed during the ski run construction is reported with a dashed black line with triangles. (b) Terrestrial view of the thermokarst depressions (photo taken by S. Ponti in 2019) in which the numbers refer to the situation of 2019 reported in Figure 7h. (c) Study site (black rectangle) in northern Italy. (d) Satellite view of the study area (source: Esri, Maxar, GeoEye, Earthstar Geographics, CNES/Airbus DS, USDA, USGS, AeroGRID, IGN, and the GIS user community) including the automatic weather stations (AWS) of Cancano (CNC) and the Share Selvio Borehole (SSB) indicated with yellow stars

Sedimentary deposits in the study area have variable grain sizes, from huge blocks of several cubic meters on the rock glacier, to gravels and pebbles with scarce sandy matrix in the Holocene tills and in the scree slopes. The thicknesses of the different deposits are almost unknown, although the thickness of the actual rock glacier exceeds 50 m.[27,28]

The ski run was built mainly using the local material after separating out large blocks (> 50 cm diameter) that were partially used for the lower basement of the ski run. The grain size of the upper 50 cm of the ski run is gravel (69.2%) with sand (29.5%) and a tiny amount of silt and clay (1.3%). The gravimetric water content ranges between 5 and 12%, and the total organic matter content is around 0.5%.

The Holocene glacial evolution of this area is not very well known. The Little Ice Age (LIA) started about AD 1560 and ended in AD 1860,[29] whereas during most of the Holocene the area was almost completely covered by the Scorluzzo Glacier and by the transfluence from the northeast of the Stelvio–Vedretta Piana glacier.[30] The Scorluzzo Glacier disappeared between 1937 and 1956.[28–31]

The climate is characterized by a continental regime,[32] with a mean annual air temperature (MAAT) around −1°C. Precipitation values are highly variable due to the complex orography, with total annual precipitation generally less than 900 mm. Snow may fall at any time of the year, covering the ground continuously for more than 6 months, from November to June.

Despite the patchy and discontinuous permafrost distribution,[33,34] at 3,000 m asl the permafrost thickness exceeds 200 m[29,35] at the Share Stelvio Borehole (SSB) site, located less than 1 km from the study site (Figure 1d). The borehole is located in a similar zone in terms of slope and elevation (around 200 m higher) to the study area. Permafrost distribution in the study area can be assumed using the Alpine-wide Permafrost MODel (APMOD,[36]). This model gives an index of permafrost probability based on mean annual air temperature, total precipitation (for the period 1961–1990) and potential incoming radiation validated through rock glaciers and other permafrost indicators available throughout the European Alps. According to that model, permafrost in the study area should be between the classes "nearly in all conditions" and "mostly in cold conditions," in which some grain-size characteristics (i.e., openwork blocks) or slope conditions (i.e., at the foot of slope) favor permafrost occurrence.

Vegetation is a mosaic of habitat types, including alpine grasslands, snowbeds, pioneer vegetation, and barren ground.[37,38] Historical data[39] and recent dendrochronological analyses indicate that the study area has been experiencing strong impacts of climate change at both the community and the species level, with an upward of migration of vegetation,[37] species turnover,[38] and shrub and tree encroachment.[40]

3 | METHODS

The present study took advantage of a multidisciplinary and integrated approach that allowed a robust geologic background definition and a geomorphologic assessment provided by the detailed geological and geomorphological survey (1:5,000 scale) performed by one of the authors (M.G.) some years ago. Geophysical methods focused on electrical resistivity tomography (ERT) and ground penetrating radar (GPR). The geophysical survey aimed specifically to: (a) investigate the subsurface, in order to discriminate between geological and glaciological features; and (b) monitor through time the evolution of the subsurface status and structures.

3.1 | Climatic data

The nearest available meteorological station with a climatic record extending over the whole examined period (since 1981) is located at Cancano (46° 31′02.2″N, 10°19′14.7″E, 1,948 m asl; Figure 1d). Here air temperature, liquid precipitation, and snow height at the ground were recorded daily. Monthly, seasonal, and annual means of air temperature and of the sum of liquid precipitation were computed for the whole period (1981–2019), and their anomalies with respect to the reference mean for the period 1981–2010 were computed. Unfortunately snow height is only indicative, because the high spatial variability and the effect of avalanches makes extrapolation of the snow height of this station problematic.

In addition, mean annual permafrost temperature at the zero annual amplitude (ZAA) reconstructed on the basis of the thermal profile at the SSB since 1981[29] was used as a proxy of the permafrost temperature in the study area.

3.2 | Field data

3.2.1 | Geophysical data

ERT surveys were performed with a Syscal Pro (IRIS International) and/or a 16G (Pasi) georesistivimeter connected to between 32 and 72 electrodes spaced 2 or 5 m apart. We repeated the acquisition in different years (from 2010 and 2019), also collecting the data in different seasons (from June to October). All the ERT measurements were acquired by means of Wenner electrode configurations in order to better highlight the main vertical variations.[41] The data were carefully edited to check the effective electric currents, the difference of potential, the apparent resistivities, and the per cent standard deviation of the different measurements taken for the same acquisition quadrupole. We then used the Res2Dinv software[42] to invert the data, setting a root mean square (RMS) convergence limit equal to 5%.[43]

The general high quality of the ERT data (except for a few profiles collected when significant snow deposits were still present) is testified to by: the values of the maximum standard deviation of original measurements (for data acquired with the same quadrupole) usually not exceeding 2%; the number of data filtered out from the original datasets never exceeding 2.6%; and the RMS error of the inversion model, which is always lower than 10% (except in the previously cited

surveys) after a maximum of five iterations, being for most of the real resistivity model lower than 4%.

It is essential to specify that, due to logistical constraints, it was impossible to leave the electrodes fixed for the repeated measurements in subsequent years and even in the same season. Therefore, both electrode location and coupling were not constant. However, before starting measuring we always checked the resistance at the electrodes, trying to minimize such a value by wetting the ground with salt water and/or using more interconnected electrodes for some specific locations.

The GPR survey was performed along the ERT profiles and following many other intersecting paths. We used a ProEx Malå Geoscience GPR instrument, equipped with 250- and 500-MHz shielded antennas in common offset configuration. GPR triggering was done by an electro-mechanical odometer, setting a constant trace interval equal to 0.1 m. A GPS device was used for both ERT and GPR positioning. The applied GPR processing flow included: DC removal, zero time correction (drift removal), spectral analysis and filtering, geometrical spreading correction, exponential amplitude correction, depth conversion, and 2D migration when highly dipping reflectors and/or scattering were present (further details of GPR data processing can be found, for instance, in Jol, 2009[44]).

3.2.2 | Topographic data

The depression edges were directly mapped in the field with a portable differential global positioning system (DGPS) Magellan ProMark 3 with a submetric absolute accuracy. The survey was repeated in 2013, 2018, and 2019 to detect changes of the depressions' shape. Edges were defined as an abrupt transition between high and low slope angle.[45]

3.2.3 | Vegetational data

The vegetation of the ski run and surrounding areas was surveyed during summer 1998 through mapping and phytosociological relevés.[37,38,46–48] In the field, uniform vegetation patches were recognized and reported on the map (at a scale of 1:2,500) and, for each mapped patch, we carried out at least one phytosociological relevé, which was randomly placed on homogeneous vegetation within each investigated patch. Each of the 45 relevés carried out provided the total vegetation coverage (%), the species list, and, for each species, its coverage that was visually estimated with a range from 0 to 100%, retaining information on lower coverage values.[37,38] The attribution of the phytosociological relevés to their community types was performed based on the occurrence of species considered characteristic of each vegetation type and whose occurrence was therefore evaluated as diagnostic to recognize the community type.[39,49,50] A principal component analysis (PCA) was performed using the software CANOCO for Windows,[51] to analyze in detail the vegetation. Data were square-root transformed, scaling was made through inter-species correlation, standardization by species was centered, and sample standardization was centered. The monitoring of vegetation colonization of the ski run was carried out after 2003–2004 (from the onset of vegetation colonization). In 2019 the vegetation survey included a remapping of the vegetation distribution and the census and dendrochronological analysis of several subalpine shrubs all belonging to the genus *Salix* occurring along the ski run and neighboring areas. Vascular plants were identified up to the species level, while cryptogams were grouped as mosses and lichens. Species determination and nomenclature was standardized following Pignatti (1982),[52] Lauber and Wagner (1998),[53] Conti et al. (2005),[54] and Wilhalm et al. (2006).[55]

3.3 | Thermokarst monitoring through remotely sensed images

The digital images used in this study consist of several orthophotos (1981, 1989, 2003, 2006, 2007, 2012, 2015) freely available at different websites and one satellite image downloaded from Google Earth (2018) (Table 1). The latter was georeferenced in ArcGIS 10.3 on the orthophoto (2015) through the selection of four control points that produced a georeferencing root mean square error (RMSE) equal to 0.59 cm. The unmanned aerial vehicle (UAV) photogrammetric survey conducted in September 2019 was used to obtain the most recent orthophoto and digital elevation model (DEM) in Agisoft Metashape 1.5 that will also be necessary for the future monitoring (Table 1). The survey consisted of a single flight of a DJI Matrice 210 RTK with a nadir photomosaic acquisition.[56] The accuracy of each image (5,280 × 3,956 pixels) followed the GPS Real-Time Kinematic (RTK) of 1 cm horizontal and 2 cm vertical accuracy, while the resolution depended on the installed camera (Zenmuse X5S, 20.8 MP, focal length 15 mm, micro 4/3 sensor). Some of the most important characteristics of the bundle adjustment are summarized in Table 2.

The relative (or geomorphological) accuracy, which is more important than the GPS absolute accuracy, was calculated as the RMSE between known and modeled distances to assess the model quality.[57] Indeed, the *in situ* measurement of height and length of nine stable boulders exterior to the thermokarst depressions yielded the RMSEs described in Table 3.

Three terrestrial thermal images were taken with a thermal camera (FLIR E85, 384 × 288 pixels, 0.1°C resolution) at the same location but at different dates to assess the differences in temperature between the depression's surface, the outer area surface, and the air. Two images were taken at the warmest moment of the day (between 1:00 p.m. and 3:00 p.m. local time on September 17 and October 17, 2018), and the third was before sunrise (8:00 a.m. local time) on August 26, 2019. Subsequently, the temperatures were averaged for each depression and its outer area through the zonal statistics tool in ArcGIS 10.3.

In addition, two ground images were taken from the northernmost part of the study area in 2003 (1,600 × 1,200 pixels) and 2018 (5,120 × 3,840 pixels) to have a different perspective of the changes in the depressions.

TABLE 1 Orthophoto and DEM resolutions, errors and sources. RMSEp = root mean square error planar, RMSEv = root mean square error vertical

	Orthophoto resolution (m)	DEM resolution (m)	RMSEp (RMSEv)	Source	Last access
1981	2.0	20.0		https://www.geoportale.regione.lombardia.it/	05-12-2020
1989	0.25			http://wms.pcn.minambiente.it/	05-12-2020
2003	1.0			https://www.geoportale.regione.lombardia.it/	05-12-2020
2006	0.25			http://wms.pcn.minambiente.it/	05-12-2020
2007	0.21			http://wms.pcn.minambiente.it/	05-12-2020
2012	0.21			http://wms.pcn.minambiente.it/	05-12-2020
2015	0.21	5.0		https://www.geoportale.regione.lombardia.it/	05-12-2020
2018	0.14*			Google Earth	
2019	0.01	0.02	0.08 (0.16)	UAV	

TABLE 2 Specifications of the photogrammetric flight conducted with the UAV

	Cameras (°N)	Flight height (m)	RMS reprojection error (m)	Dense cloud points (°N)	GSD (mm)	Image overlap (%)	Reprojection of tie points (pixels)
UAV survey	81	45	0.32	2.5×10^8	9.4	70	0.7–2.5

TABLE 3 Errors obtained by comparing the three different methods to measure the depressions (GPS tracking, orthophoto polygoniving, DEM shading) in 2019. The values refer to the standard deviations of measurement units (m and m^2)

Thermokarst ID	Length (m)	Width (m)	Depth (m)	Perimeter (m)	Area (m^2)
1	0.59	0.25	1.46	1.08	1.96
2	2.72	1.91	0.21	52.31	318.02
3	2.17	0.72	0.75	50.10	138.28
4	2.98	3.50	2.12	9.67	72.22
Average	2.11	1.60	1.13	28.29	132.62

The 2019 DEM and orthophoto were used to detect the edges of the depressions and also compared with the 2019 GPS track to provide the most accurate method of monitoring the evolution of thermokarst landforms. When the DEM was available (2019), the DEM shading at different azimuth angles[58] helped to better visualize the edges,[45] otherwise the depressions were manually polygonized in ArcGIS 10.3 from the orthophoto. Edge delineation on the older orthophotos was possible due to the depression slope, because on a grayscale band, the direct irradiance along the edges produced darker (shadow) and brighter (direct irradiance) values compared to the exterior. Thus, the depression boundaries were set where both brighter and darker values occurred. Subsequently, the polygonized depressions were enclosed in a minimum bounding rectangle that permitted calculation of their length and width (m) in ArcGIS 10.3 (Table 4). To

TABLE 4 Measurements of length (L) and width (W) (in m) of the thermokarst depressions from the orthophoto polygonizing in the period 1989–2019. Blank cells indicate when the depressions coalesced (2a–c, 3a)

	1989		2003		2006		2007		2012		2015		2018		2019	
Depression	L	W	L	W	L	W	L	W	L	W	L	W	L	W	L	W
1	0	0	11.9	7.5	14.1	7.5	14.9	7.5	15.8	9.9	15.8	10.4	15.8	11.5	22.7	12.5
2	0	0	16.2	10	16.3	10	16.3	9.8	20.4	10.3	20.2	11	20.2	14	47.6	37.6
2a	0	0	18.5	8.5	18.5	12.7	18.3	12.7	27.7	13.7	30.4	17.5	31.7	17.5		
2b	0	0	9	7.1	12.7	8.4	14.7	8.4								
2c	0	0	8.8	6.3	15.5	9.2	17.4	9.2	17.2	10.9	18	15.3	20.3	15.2		
3	0	0	0	0	0	0	0	0	10.1	6.2	13.5	9.9	22	11.3	30.3	21.5
3a	0	0	0	0	0	0	0	0	9.8	7.8	11.9	8.5	12.6	8.5		
4	0	0	0	0	0	0	0	0	13.9	9.5	17.6	11.6	17.6	11.6	20.1	14.4

locate the study area in terms of permafrost distribution, the Alpine-wide Permafrost MODel (APMOD) model[36] was used as a raster layer in ArcGIS 10.3.

4 | RESULTS

4.1 | Climate

Since 1981 at Cancano AWS (Figure 1d), MAAT showed a statistically significant warming (β = +0.038; R = 0.57; p < 0.05) that has been mainly concentrated in summer (June–July–August; β = +0.065; R = 0.65; p < 0.05). Indeed, in the first decade (1981–1990) mean summer air temperature was 10.5°C, whereas it rose to 12.2°C (with an increase of +1.7°C) in the last 10 years. Despite this clear warming trend, the interannual differences were very strong, with the summer 2003 being particularly hot (+14.7°C, which is 3°C more than the average of the examined period) followed by 2019 (+13.5°C, Figure 2). Interannual variability was even stronger considering the total annual precipitation, with 1,250 mm in the wettest year (2000) vs. 550 mm in the driest (2005) (Figure 2).

4.2 | ERT and GPR investigations

ERT inverted models highlighted interesting features that are synthetized in Figure 3, in which all profiles were plotted with the same resistivity range, thus allowing an easier comparison.

Longitudinal ERT profiles show variable resistivity close to the topographic surface, with values ranging from about 300 to more than 10,000 Ωm. Such an extremely high range was more apparent in both early and late summer, while during August the range was lower. This was probably related to local snow deposits responsible for high resistivity in early summer, or to local freezing close to the surface during September (and the following months). Deeper in the profiles were noticeable lateral resistivity variations, with the central zone always showing low resistivity values (<1,000 Ωm) and higher values towards both the north and the south. In the profile of September 2014 such zones exhibited values exceeding 10,000 Ωm. This was not the case in both 2017 and 2019, whereas in August 2018 the resistivity values were always higher than in August 2019. The central low-resistivity zone shows very similar resistivity values through time, with highly conductive materials typical of the schists cropping out in the area.

Transverse (east–west) ERT profiles highlighted a peculiar situation with strong lateral variations in the early measurements (until 2013), and a more homogeneous distribution in the more recent surveys. Figure 4 compares two profiles collected in 2010 and 2019, both considering the topography at the acquisition time and carried out almost in the same period of the year (late July and early August, respectively). The profiles show a decrease of one order of magnitude of the resistivity in the southern zone between 2010 and 2019.

The penetration depth of the GPR signal was often limited, even using relatively low-frequency antennas, and the diffuse scattering prevents the imaging of structures deeper than 3–5 m. However, the comparison between profiles collected along the same paths in different periods (or even years) allowed detection of some cryotic features.

Figure 5 provides an example of the 250-MHz profiles collected in June and August 2017. Although some subsurface structures were almost identical on both records, and were therefore interpreted as stratigraphic or geological structures, others occurred only in the earliest profile, when the snow patches were present on the surface.

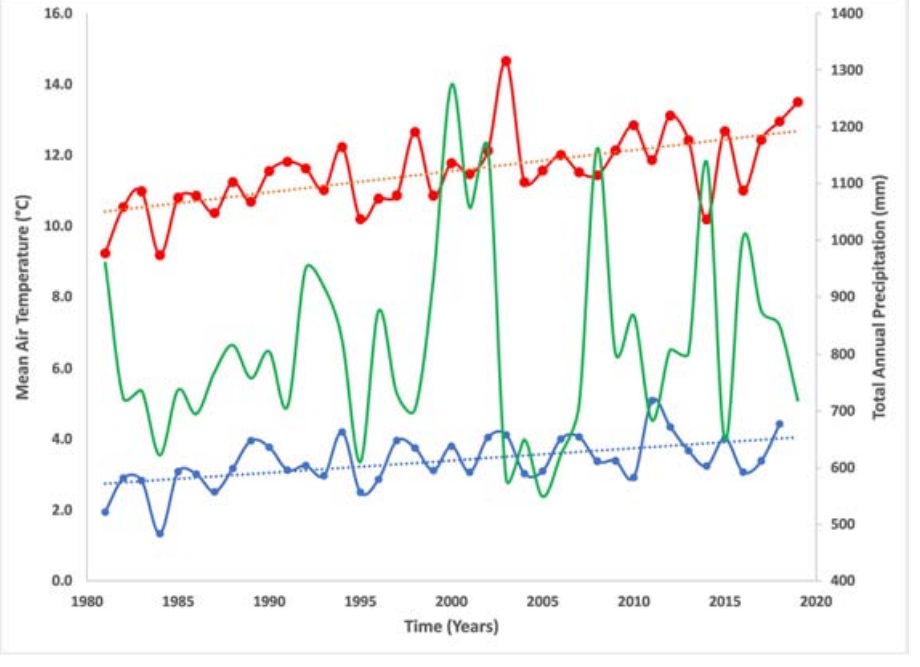

FIGURE 2 Climate at the Cancano automatic weather station (see Figure 1 for location). The increase in mean summer air temperature (June–July–August; red line) is confirmed also by the linear regression (dashed red line), whereas the mean annual air temperature (MAAT, blue line) showed slightly less warming than summer temperature. Total annual precipitation (green line) did not show any trends but very large annual fluctuations

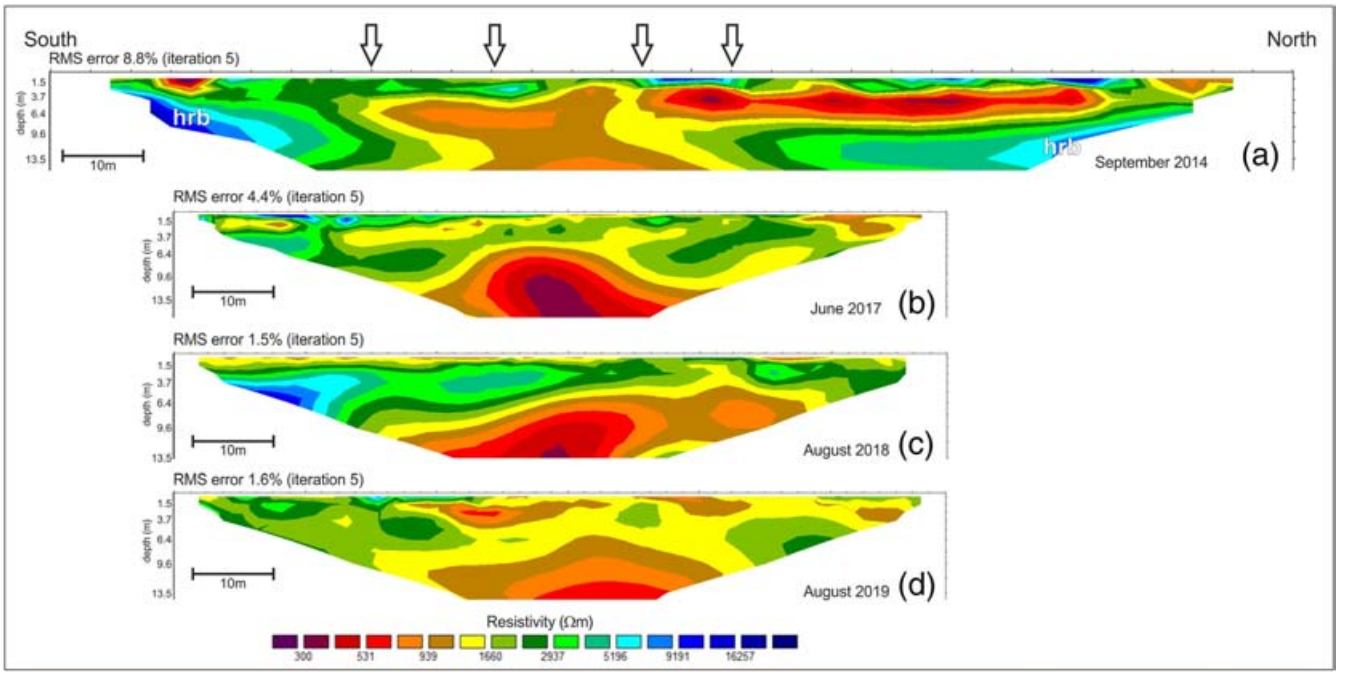

FIGURE 3 South–north ERT inverted profiles across the thermokarst depressions. (a) September 2014; (b) June 2017; (c) August 2018; (d) August 2019. All pictures have the same scales and are plotted with the identical resistivity color bar. Black arrows mark the approximate location of thermokarst depressions crossed by the profiles; hrb label in (a) highlights high-resistivity zones

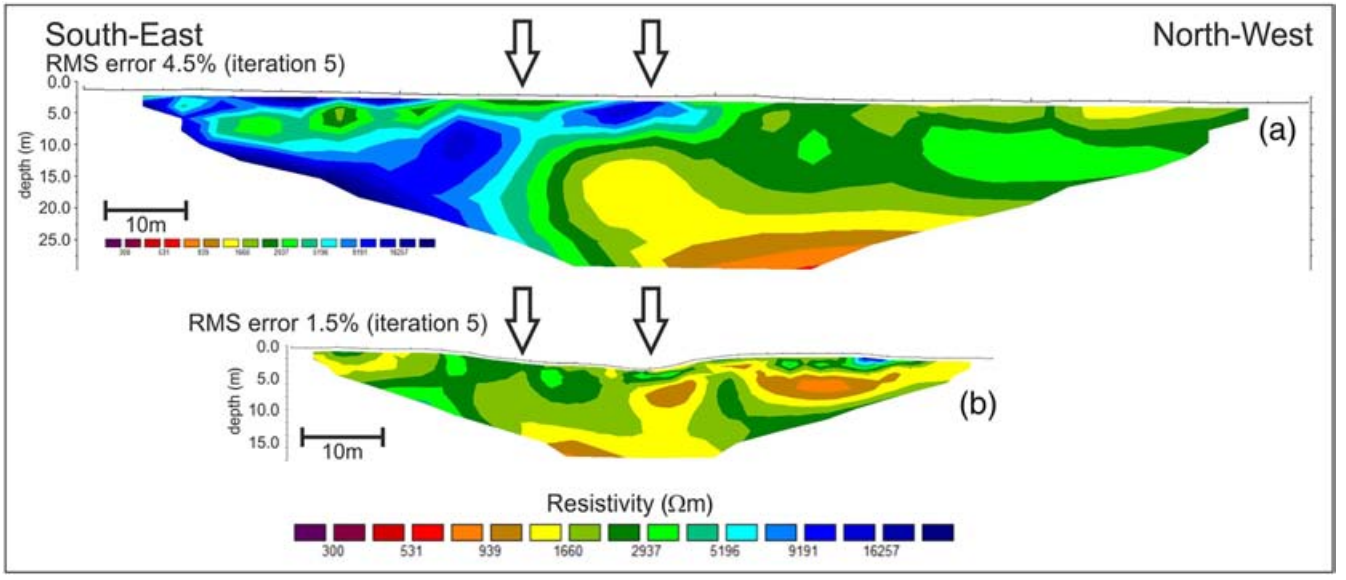

FIGURE 4 SE–NW inverted profiles across the thermokarst. (a) July 2010; (b) August 2019. Both pictures have the same scales and are plotted with the identical resistivity color bar. Black arrows mark the approximate location of thermokarst depressions crossed by the profiles

4.3 | Thermokarst monitoring

Based on the remote sensing images integrated with the field surveys, the first thermokarst depressions developed between 1999 and 2003. In 1998, when the first ERT measurements were performed during the EU PACE project (Permafrost and Climate in Europe), the surface of the ski run was still undisturbed. By 2003, five thermokarst depressions were recorded (numbered 1, 2, and 2a–c in Figures 6a,b and 7b) and remained almost unchanged until 2007 (Figure 7c,d). Between 2007 and 2012, three new thermokarst depressions (3, 3a, and 4) progressively developed towards the higher elevations along the steeper part of the ski run, with the coalescence of the older depressions 2a and 2b (Figure 7e). After 2012 and until 2018 the depressions remained almost unchanged (Figure 7f,g), although

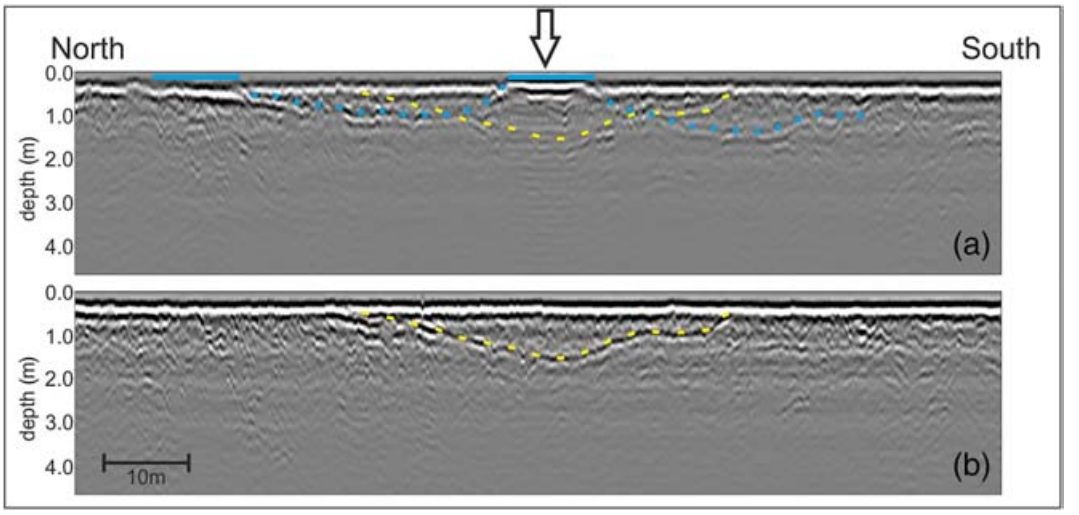

FIGURE 5 Comparison between two 250- MHz GPR profiles collected in June 2017 (a) and August 2017 (b). The yellow dashed lines highlight particular geological horizons, while the blue dotted line marks the top of the frozen materials. The continuous blue lines correspond to two shallow snow deposits; the black arrow marks the approximate location of a thermokarst depression crossed by the profiles

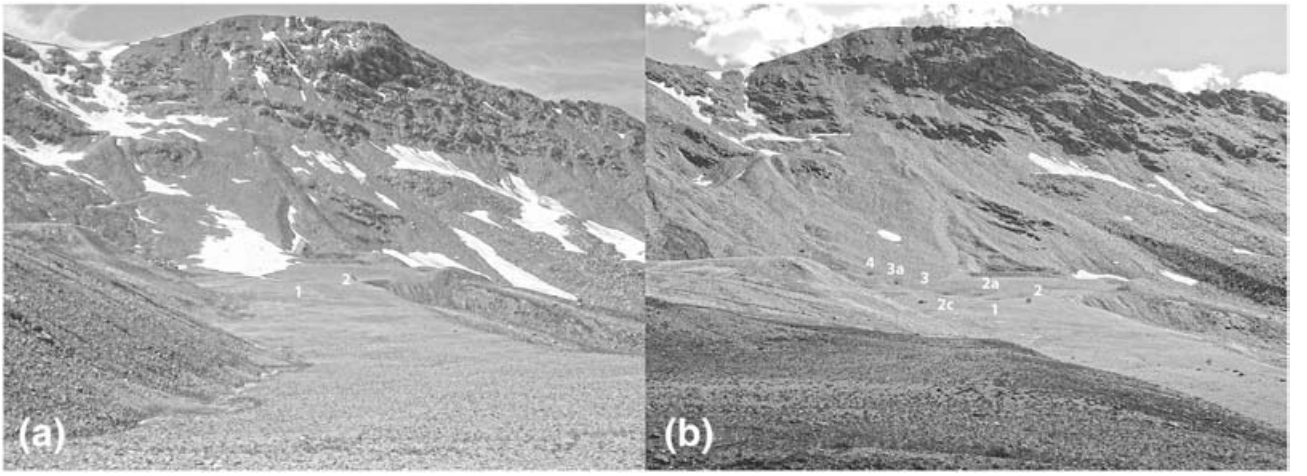

FIGURE 6 Comparison between terrestrial views of the ski run in (a) late June 2003 and (b) July 2018 with the thermokarst depressions numbered. Note that in 2003 only two depressions (1 and 2) were visible, whereas the other three (2a, b, c) were completed covered by long-lasting snow

between 2018 and 2019 the coalescence of depressions 2 (2a + 2b) and of 3 with 3a resulted in four larger depressions (1, 2, 3, and 4; Figure 7h).

Comparing all the available different measuring methods of the depressions (GPS tracking, orthophoto polygonising, DEM shading), only in 2019 did the length and width of the features (Table 3) show a higher consistency through the different measurement techniques (on average <2.5 m). Therefore, only the lengths and widths of different years have been compared to understand their temporal changes.

The DEM was available only for 2019 and therefore it was not used for the temporal analysis. With regard to the lengths and widths, the orthophoto polygonizing showed larger changes during 2018–2019 (average length and width of 7.9 and 8.4 m, respectively) than the GPS tracking (average length and width of 7.1 and 6.8 m, respectively). Thus, mapping the depressions through the orthophotos was considered to be the best method, even though the resolution of the images was not constant. Additionally, the time sequence of the orthophotos was longer than the GPS tracking (started in 2013).

Analyzing the aerial photographs available before construction of the ski run, only the image for 1981 (Regione Lombardia) had sufficient resolution for the analysis. Comparing such images with the orthophotos taken soon after the construction of the ski run in 1987, the area currently occupied by the thermokarst depressions was the central-frontal part of an active rock glacier (Figure 8) where, during the excavation, massive ice was found at a few meters depth (U. Capitani, personal communication).

To reveal the local surface thermal conditions induced by the thermokarst depressions, some terrestrial thermal images were

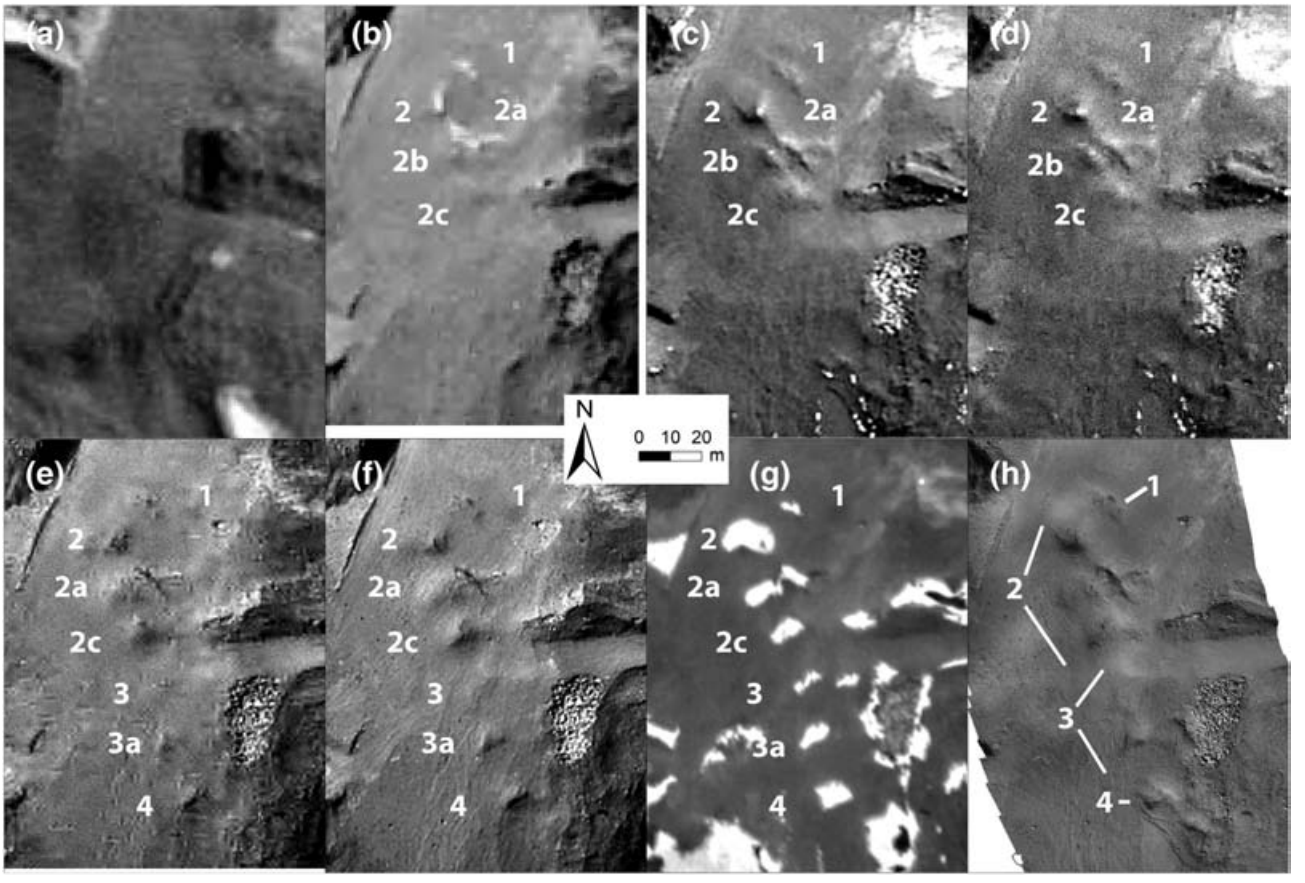

FIGURE 7 Time sequence of orthophotos (a) to (f) and (h), and a georeferenced image (g) showing the temporal evolution of thermokarst depressions: (a) 1989, (b) 2003, (c) 2006, (d) 2007, (e) 2012, (f) 2015, (g) 2018, (h) 2019. Numbers 1 to 4 indicate the depressions. Depressions 1 and 4 remained almost unchanged through time, although the latter appeared only in 2012. Of note also are the processes of coalescence that affect the other depressions

recently (since 2018) obtained in summer during times of minimum and maximum heating. The images show that when the area was snow-free the thermokarst depressions were characterized by higher ground surface temperatures than the outer areas, especially in October, and to a less extent in September and August (Table 5 and Figure 9).

4.4 | Vegetation development

In 1998 data from 45 phytosociological relevés were obtained to map the vegetation in the ski run and surrounding areas. PCA identified two main vegetation communities, the pioneer vegetation (*Oxyrietum digynae*) and the snowbed vegetation (*Salicetum herbaceae*), and the transition between them (Figure 10, Table 6). Among the relevés belonging to the pioneer vegetation, the PCA highlighted the occurrence of relevés dominated by different characteristic species, including *Ranunculus glacialis*, *Geum reptans*, and *Saxifraga bryoides*, which were more abundant, and of other species typical of the pioneer communities such as *Cerastium uniflorum*, *Oxyria digyna*, and *Cardamine resedifolia*, whereas the most abundant snowbed species were *Veronica alpina* and *Cerastium cerastioides* (Figure 10, Table 6). The relevés on the ski run were all located (overlapping) on the right side of the graph, as all of them are characterized by a lack of vegetation (Figure 10, Table 6). According to the results of the field survey and of the PCA, the phytosociological map shows that in 1998 (i.e., almost 10 years after ski-run construction) the ski run was totally devoid of vegetation. The ski run area lacked vegetation until 2003–2004.

The vegetation survey indicated that, in 1998, two main vegetation types (pioneer vegetation and snowbed vegetation) colonized the undisturbed area around the ski run (Figure 11a). In the undisturbed area at higher elevation than the ski run, discontinuous pioneer communities occurred, with the dominance of the association *Oxyrietum digynae* in pure stands (characterized by the occurrence of *Ranunculus glacialis*, *Saxifraga bryoides*, *Cerastium uniflorum*, *Leucanthemopsis alpina*, *Poa alpina*, *Geum reptans*, and *Oxyria digyna*) as well as in transition with the snowbed association *Salicetum herbaceae* (with the occurrence of *Veronica alpina* and *Cerastium cerastioides*) (Figure 11a). The undisturbed area located at lower elevation than the ski run was characterized by the snowbed vegetation (*Salicetum herbaceae*), in its typical form, with the ingression and dominance of *Salix herbacea* and

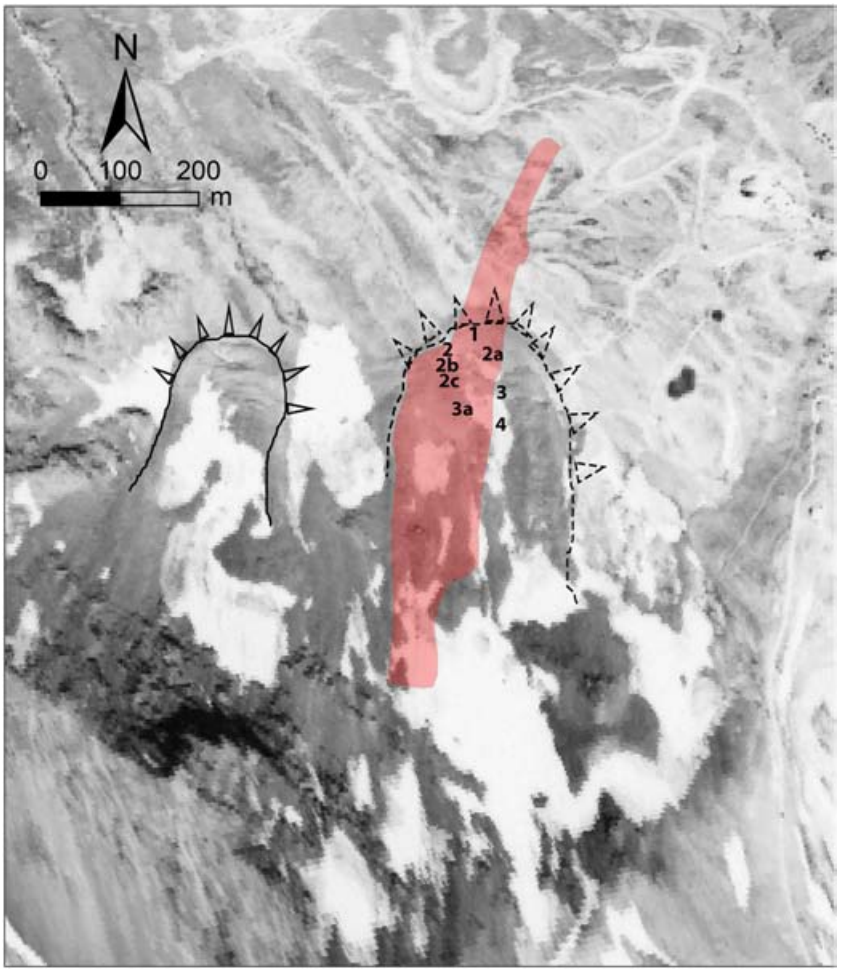

FIGURE 8 Aerial photograph of the study area in 1981 before construction of the ski run. Two neighboring active rock glaciers are visible: The rock glacier on the right (dashed black lines with empty triangles) was destroyed during construction of the ski run, whereas the one on the left remains today (solid black line with triangles). The red polygon indicates the ski run built between 1987 and 1991. The thermokarst depressions developed after 1998 are numbered in black

TABLE 5 Thermal differences expressed as mean temperature (°C ± standard deviation) at the ground surface between the internal and external parts of the depressions at different dates. For comparison, air temperature recorded simultaneously is also shown. In 2018 the acquisition time refers to the maximum incoming radiation (early afternoon), whereas in 2019 it refers to the minimum (before sunrise)

Depression	17-09-2018 (°C)	17-10-2018 (°C)	26-08-2019 (°C)
1	2.2 ± 1.2	3.0 ± 2.6	0.9 ± 1.3
2	2.4 ± 1.8	3.6 ± 3.5	2.8 ± 2.6
3	0.9 ± 1.4	1.1 ± 3.1	1.4 ± 2.3
4	1.2 ± 1.2	4.1 ± 3.2	1.1 ± 2.5
Air	10.3	9.4	9.3

of the alpine grassland with its climax association (*Caricetum curvulae*) (Figure 11a).

Between 2004 and 2010 vegetation colonized the ski run area (Figure 11b). At the beginning single individuals of *Androsace alpina*, *Arabis alpina*, *A. coerulea*, *Linaria alpina*, and *Saxifraga oppositifolia* initiated the vegetation succession (Figure 11c) (with the earliest pioneer association *Androsacetum alpinae*), with scattered and discontinuous coverage (< 1%). The succession evolved with the ingress of *Geum reptans*, *Leucanthemopsis alpina*, and *Poa laxa* and a coverage increase (up to 5%–10% in some localized patches), indicating the onset of its evolution from *Androsacetum alpinae* to the following successional stage of pioneer vegetation (*Oxyrietum digynae*).

After 2011 the vegetation succession on the ski run developed more rapidly (Figure 11b). Ingress occurred of several other pioneer species (*Cerastium uniflorum*, *Saxifraga bryoides*, *Cirsium spinosissimum*, *Gentiana bavarica*) typical of the association *Oxyrietum digynae*, and of early-successional species (*Doronicum clusii*, *Luzula alpino-pilosa*) typical of the association *Luzuletum spadiceae*, as well as of snowbed (*Salix herbacea*, *Veronica alpina*) (Figure 11d) and alpine grassland species (*Senecio incanus* subsp. *carniolicus*, *Trifolium badium*), with a discontinuous coverage up to 25–30%. The pioneer vegetation was distributed along the whole ski run.

Since 2004 the lower part of the ski run area (from the road up to the area near the thermokarst) was progressively colonized

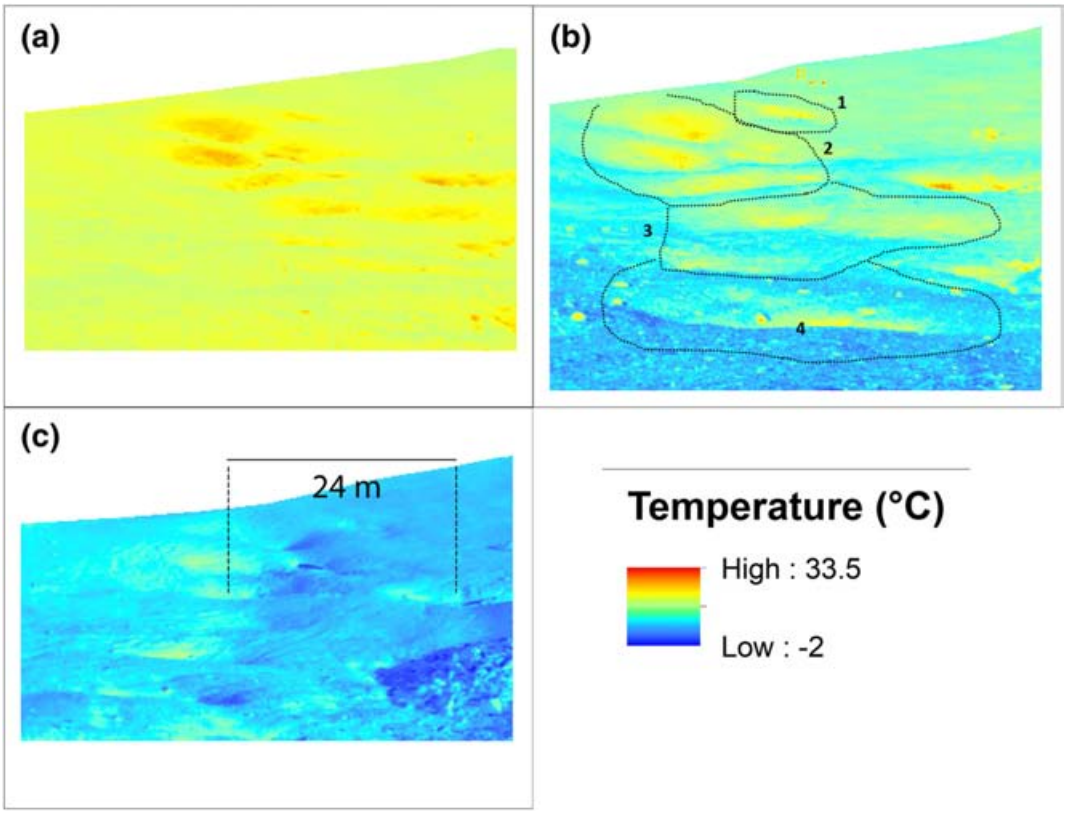

FIGURE 9 Surface temperature of the depressions on different dates and times of day revealed by thermal terrestrial acquisition: (a) September 17, 2018 3:00 p.m., (b) October 17, 2018 2:00 p.m., (c) August 26, 2019 8:00 a.m. Numbers 1–4 refer to the depressions described in Figure 7 and Table 3

by several subalpine *Salix* shrubs. The earliest colonization was recorded for *S. breviserrata* (2004), followed by *S. helvetica* (2005), *S. waldsteiniana* (2006), *S. hastata* (2007), *S. foetida* (2009), and *S. glaucosericea* (2012). In total, 111 individuals of the different *Salix* species were recorded along the ski run (Figure 11b, blue dots).

Colonization of the thermokarst depressions started with the species typical of the earliest stages of succession (*Androsace alpina*, *Arabis alpina*, *A. coerulea*, *Linaria alpina*, *Saxifraga oppositifolia*). Vegetation development towards more mature successional stages was much slower in the depressions than on the surrounding ski run, as it was characterized by lower species richness and vegetation coverage and occurrence of vegetation communities typical of earlier successional stages (*Androsacetum alpinae*) compared to those of the ski run (*Oxyrietum digynae)*. Only in the last couple of years has the vegetation succession within the depressions evolved further. In particular, the depressions are currently colonized by pioneer species (*Cerastium uniflorum*, *Cardamine resedifolia*, *Leucanthmopsis alpina*, *Poa alpina*) and snowbed species (*Arenaria biflora*, *Veronica alpina*, *Gnaphalium supinum*) with coverage between less than 10% and 60%. Depression 2a shows a continuous moss coverage belonging to the snowbed association *Polytrichetum sexangularis*, typical of the latest melt of the snow cover.

5 | DISCUSSION

5.1 | Thermokarst formation

As discussed above, thermokarst depressions can form by several processes influenced directly by different sources of heat and types of ground ice, and therefore indirectly by the host deposits and relief morphology (i.e., Jorgenson, 2013).[7] In the present study, the artificial deposits are mainly composed of gravel (69.1%) and sand (29.5%) that are well compacted (as testified by the quite low gravimetric water content, ranging between 5% and 12%). These characteristics suggest that interstitial ice should dominate, although some segregated ice cannot be excluded. The relief characteristics (a relatively steep slope and its foot followed by an almost subhorizontal surface), the absence of rill erosion or gully erosion on the ski run surface, as well as the presence of small artificial channels on the side of the ski run collecting the running water suggest that air warming or, more likely, disruption of the thermal equilibrium of permafrost (due to variation of the surface energy balance) was the main cause for the formation of the thermokarst depressions developed in the last 20 years.

According to the classification proposed by Jorgenson (2013),[7] the depressions analyzed in the present paper may relate to the thaw pits or to thaw slides, depending on their position (depressions 3 and

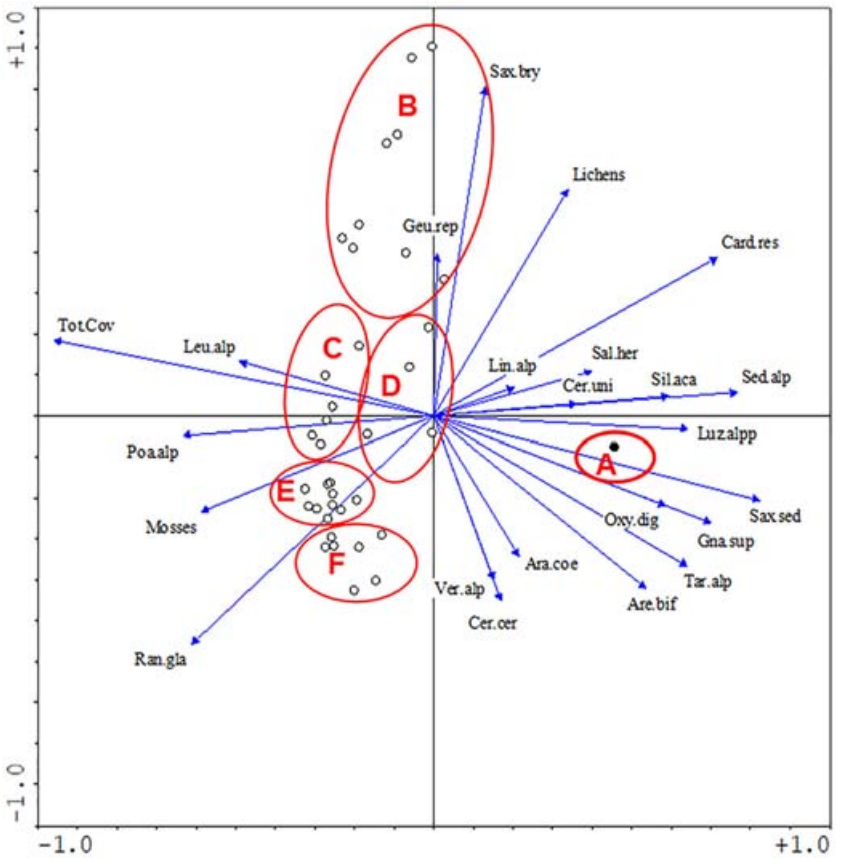

FIGURE 10 Biplot of the multivariate analysis (PCA) showing the plots (dots; the black dot indicates the plots with barren ground) and the vegetation characteristics. Legend: Ara.coe = *Arabis coerulea*; Are.bif = *Arenaria biflora*; Card.res = *Cardamine resedifolia*; Cer.cer = *Cerastium cerastioides*; Cer.uni = *Cerastium uniflorum*; Geu.rep = *Geum reptans*; Gna.sup = *Gnaphalium supinum*; Leu.alp = *Leucanthemopsis alpina*; Lin.alp = *Linaria alpina*; Luz.alpp = *Luzula alpino-pilosa*; Oxy.dig = *Oxyria digyna*; Poa.alp = *Poa alpina*; Rang.gla = *Ranunculus glacialis*; Sal.her = *Salix herbacea*; Sax.bry = *Saxifraga bryoides*; Sax.sed = *Saxifraga sedoides*; Sed.alp = *Sedum alpestre*; Sil.aca = *Silene acaulis*; Tar.alp = *Taraxacum alpinum*; Ver.alp = *Veronica alpina*. PCA groups A–F are detailed in Table 6

4 are on a slope, whereas depressions 1 and 2 are on a subhorizontal surface). The absence of ponds is related to the probably high hydraulic conductivity of the artificial deposits, their relatively low ice content, and their very recent formation. In depression 2a, for example, a small pond occurred in some years and a moss carpet 2–3 cm thick has been established. Another potential source of ice could be remnants of buried massive ice that was found during the destruction of the active rock glacier still visible in the aerial photographs of 1981 (U. Capitani, personal communication). Indeed, Figure 8 clearly shows that all the depressions are in the frontal part of the former rock glacier. Moreover, in the remaining active rock glacier close to the ski run, Guglielmin (1994)[27] revealed a body of probable massive ice near its front, with a thickness between 13 and 15 m, and a resistivity around 100 kΩm, underlying an active layer thickness (ALT) of between 2 and 3 m, through three different vertical electric soundings (VESs) carried out in 1993 (see Figure 1a for the location of the center of the longest VES). Later, in 1998 Cannone et al.[28] found higher resistivity values (up to 500 kΩm), but with a thicker ALT in the frontal part.

If we consider the APMOD,[36] both rock glaciers and their surrounding area in 1981 were at the limits between permafrost in nearly all conditions and permafrost mostly in cold conditions (Figure 12). Therefore, when the ski run was constructed between 1987 and 1991, the area experienced permafrost conditions, although in the lower parts (the subhorizontal part of the ski run) the model predicts permafrost mostly in cold conditions. According to Boeckli et al.,[36] the part of the ski run at the foot of the slope (depressions 1 and 2 of Figure 7h) was under favorable conditions for the formation of permafrost.

In the same area of thermokarst depressions 1 and 2, Cannone et al.[28] in 1998 (see the orange line in Figure 1a for location) found the deepest body of high resistivity (20 m): indeed, the first ERT profile revealed a body with a thickness of 10 m of high resistivity (10–30 kΩm) above 2,720 m asl and a body twice as thick as the former below 2,690 m asl in the zone between the slope and the flat area of the ski run. The active layer at that time was not easy to detect, but a reasonable estimate is that it was between 3 and 5 m thick.[24]

Considering the overall low water content of the compacted deposits along the ski run, and the relatively high electrical resistivity values found also in 1998 by Cannone et al.,[28] although there are no direct measurements of the ice content within the ski run, we can reasonably estimate a maximum ice content not exceeding 30% in volume.

5.2 | Active-layer thickening and progressive permafrost reduction

Construction of the ski run dramatically changed the surface characteristics in terms of grain size, slope, and vegetation. Indeed, the area containing the thermokarst depressions corresponded to the frontal part of the former rock glacier, which was characterized by a coarse

TABLE 6 Mean floristic composition of the vegetation communities identified by principal component analysis. Legend: OD = *Oxyrietum digynae*; SH = *Salicetum herbaceae*

PCA group	A	B	C	E	F	D
Community type	Bare ground	OD	OD/SH	OD	OD	OD/SH
Total cover (%)	0	58.3	67.5	67.	22.1	57
Androsace alpina				0.6		
Gentiana bavarica		0.01				1
Silene acaulis		1.7		0.6		
Linaria alpina		2.2	1.68	3.9	0.71	
Cerastium uniflorum		1.7		3.9		
Oxyria digyna		0.01	0.83	1.7		
Geum reptans		**5.2**	**7.5**	**5**	0.01	
Saxifraga bryoides		**20**		0.6		
Ranunculus glacialis		**5.2**	**17.5**	**16.7**	**10**	2
Cardamine resedifolia		1.7				1
Saxifraga oppositifolia		0.6		0.01		
Doronicum clusii		0.01	0.02	0.01		
Luzula alpino-pilosa						5
Leucanthemopsis alpina		**8.6**		**12.8**	**3.6**	**16.7**
Poa alpina		**7.8**	**13.3**	**15.6**	**7.2**	**4**
Salix herbacea		0		0.01		**26**
Veronica alpina		1.11	7.5	1.1	0.7	2
Cerastium cerastioides				1.1	0.03	8.33
Alchemilla pentaphyllea						
Arenaria biflora			5	0.6		
Sagina saginoides				0.01		
Gnaphalium supinum			3.33			0.02
Taraxacum alpinum			2.5	0.01	0.03	1
Arabis alpina				0.6		
Arabis coerulea			5.85	2.2	0.01	2
Sedum alpestre		0.6				2
Senecio carniolicus		0.6				
Saxifraga sedoides				0.56		0.02
Homogyne alpina						0.02
Cardamine bellidifolia						0.02
Hieracium glaciale						1
Mosses		9.4	14.1	17.2	6.4	15
Terricolous lichens		7				13

blocky surface with several troughs and ridges, and avoided by vegetation. These natural characteristics were more favorable to the permafrost conditions than those of the anthropogenic surface of the ski run (gravel with compacted sand, smooth surface, and scattered vegetation). Therefore, melt of the remaining ice originally enclosed in the rock glacier was also favored by the surface changes.

Moreover, climate change since building of the ski run has influenced the development of the thermokarst depressions through progressive melting of the ice within permafrost in the area. The trend of permafrost temperature can be represented by the deepest (235 m) permafrost borehole in the European mountains (SSB, see Figure 1; located at an elevation of 3,000 m asl) that, despite the high variability of permafrost distribution and thermal regime in alpine environments, can be considered representative of terrain less than 1.5 km away. Additionally, there is a good fit between its annual rate of permafrost temperature change (measured close to the depth of zero annual amplitude (DZAA) at 20 m) and the evolution of the thermokarst depressions (Table 7). Indeed, it is apparent that when the annual rate of increase of the permafrost temperature close to the DZAA (20 m depth) was higher, new thermokarst depressions or greater enlargement of existing depressions occurred. According to the reconstruction of the last 40 years of permafrost temperature[29] (Figure 13), a rapid and abrupt increase of permafrost temperature was recorded at SSB (more than 0.8°C per decade) between 1990 and

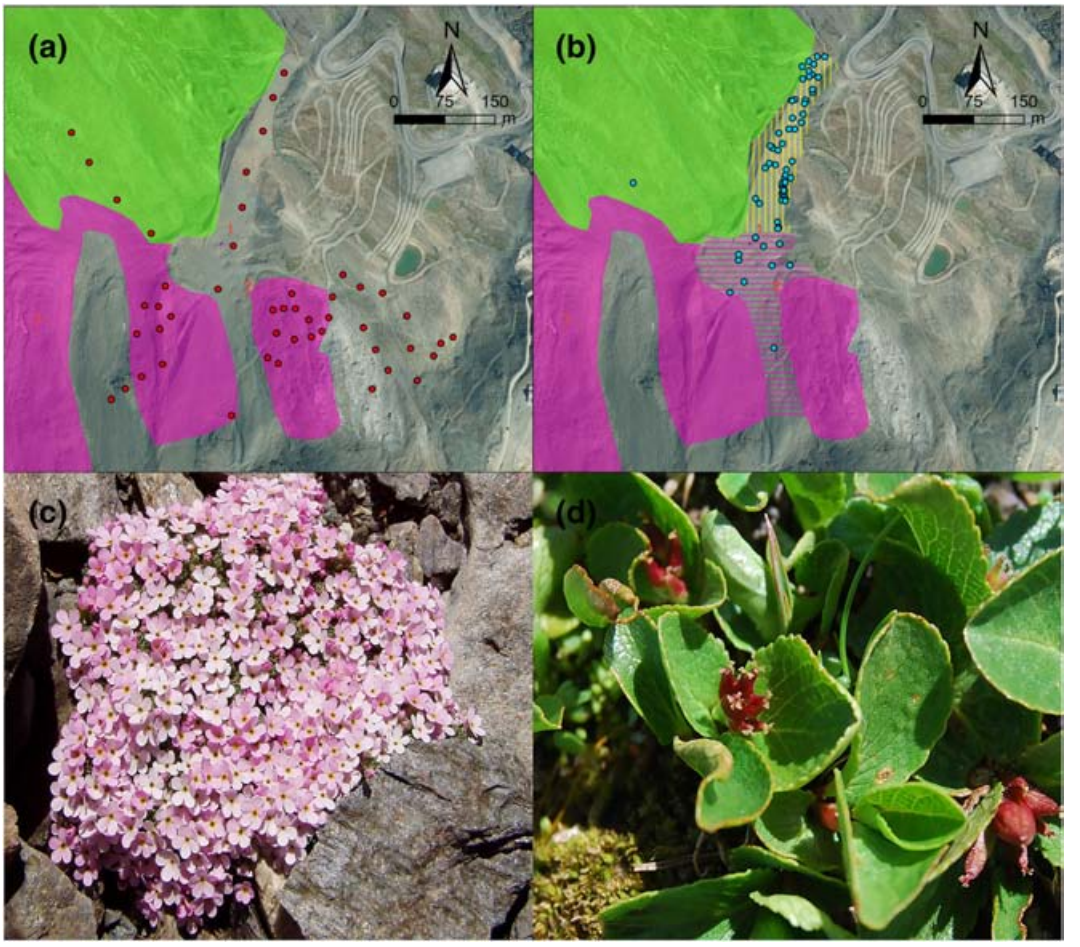

FIGURE 11 Patterns of spatial distribution and dynamics of the vegetation communities along the ski run and neighboring areas. (a) Vegetation occurrence in 1998, about 10 years after the ski-run construction, showing the ski run devoid of vegetation, the neighboring undisturbed areas vegetated with pioneer communities (pink areas) and snowbed communities (green area), and the location of the phytosociological relevés (red dots). (b) Vegetation occurrence in 2020, after initial colonization started in 2003–2004; since 2011 the ski run has been characterized by the occurrence of two different stages of pioneer vegetation (the earliest stage *Androsacetum alpinae*—area with horizontal pink lines, the following stage *Oxyrietum digynae*—area with vertical yellow lines) and the location of the *Salix* shrubs (pale blue dots). (c) The pioneer species *Androsace alpine*. the(d) The snowbed species *Salix herbacea*. Images reported in (a) and (b) were taken from the orthophoto of 2015 (https://www.geoportale.regione.lombardia.it/)

2011[29] roughly doubling the MAAT increase recorded at the Cancano AWS, considering that the ground surface reflects not only air summer warming (see Figure 2), but also summer radiation.

Just 10 m from the SSB borehole, in another, shallower borehole (10 m deep) drilled for the PACE project, ALT monitoring has been continuous since 1998 (Figure 13). Since then, ALT has been statistically significant (β = 6.89; R = 0.8; p < 0.05) and rapid (+7 cm per year) (see also Etzelmuller et al.[59]).

Considering the available geophysical investigations, which unfortunately are not continuous, both Figures 3 and 4 indicate permafrost degradation. Indeed, if we compare these profiles with the ERT reported by Cannone et al.[28] for 1998, it is evident that some ice was still present in the lower part of the ski run until 2014 (hrb label on Figure 3a), and that until 2010 the thickness of the high-resistivity body was very similar to that found in 1998 (although with a slightly lower resistivity equal to 10–20 kΩm).

If we assume that the trend of permafrost temperature in the ski run area followed a pattern similar to that reconstructed and measured at SSB, the permafrost temperature reached a maximum in 2011 and then remained almost stable until 2018. In 2019 it increased again.

The evolution of the thermokarst depressions fits quite well with the trend of the permafrost temperature recorded at SSB, although a local difference related mainly to the late-laying snow accumulated by snow avalanching induced some moderate discrepancies.

According to the climatic reconstruction, the minimum temperature at SSB immediately followed construction of the ski-run, favoring permafrost formation and the conservation of the remaining massive ice related to the previous rock glacier. Since 2002, when the permafrost temperature at the SSB was higher than −2°C, and after more than 10 years of exposure to air warming, the thermokarst depressions started to develop and progressively

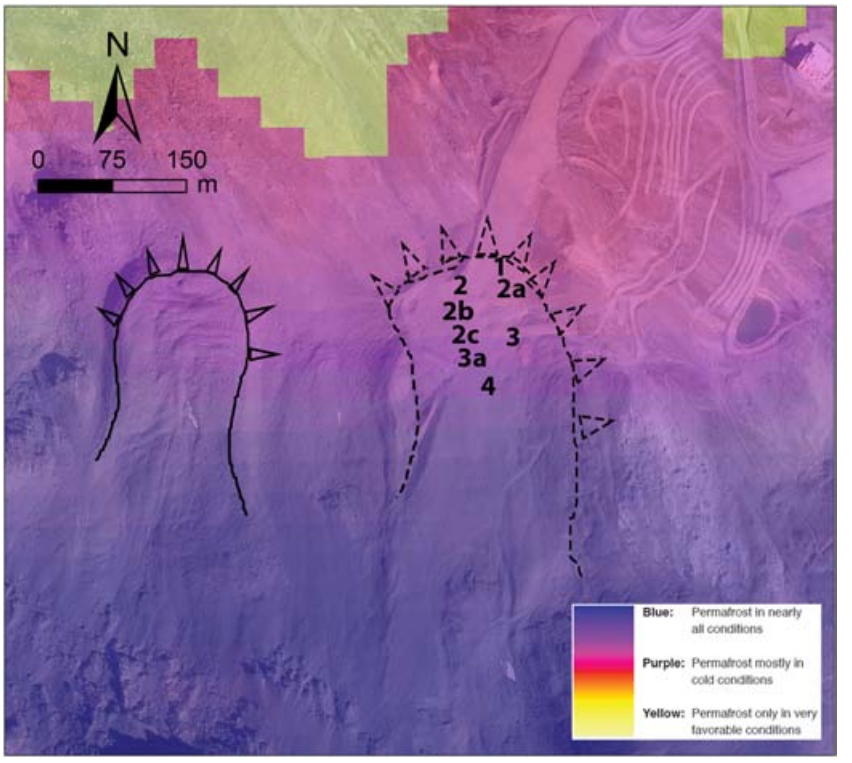

FIGURE 12 Permafrost distribution according to Boeckli et al.[36] It is notable as the thermokarst depressions (numbered in black) are in the area in which permafrost should be mostly in cold conditions and within the area of the former active rock glacier (dashed black line with empty triangles). The remaining active rock glacier is also underlined by the black solid line with triangles

TABLE 7 Annual rate of permafrost temperature changes close to the DZAA (20 m depth) at SSB and change of thermokarst depressions on the ski run

	Annual rate of permafrost temperature change at 20 m depth at SSB (°C/yr)	Degree of change of thermokarst depressions at the ski run
1999–2003	0.09	Very high (five depressions formed)
2004–2007	0.01	Very low (depressions almost unchanged)
2008–2012	0.05	High (new depressions 3, 3a and 4 formed)
2013–2018	<0.01	Very low (depressions almost unchanged)
2018–2019	0.05	High (coalescence of several depressions)

enlarged their area and extended their location towards higher elevations until 2011–12. Between 2012 and 2015 the depressions developed more slowly, whereas in the last few years their size has increased and probably these last thermokarst modifications can be related to local conditions (as underlined by Figure 9 and Table 5). In detail, when the ski run area was snow-free the thermokarst depressions were characterized by higher surface temperatures than the outer areas, especially in October, and to a lesser extent in September and August (Figure 9). On the other hand, in June and July the depressions were filled by snow cover for a longer time (Figure 6), with a net local cooling effect.

5.3 | Relationships between vegetation, climate, and permafrost degradation

Ski runs are hostile environments, requiring decades or longer for plant establishment following the natural dynamics of primary succession, as vegetation develops very slowly with low coverage (e.g., [60–62]). Given the very slow renaturalization, partial ecosystem recovery is often achieved in two to three decades through specific actions (such as machine-grading, storage and re-use of topsoil, hydroseeding of commercial seed mixtures, application of manure soon after seeding, and low-intensity grazing).[60–62] However, at high altitudes ski-run recovery and revegetation becomes increasingly difficult.[60] Our data confirm that the spontaneous revegetation of a ski run at high elevations is difficult, with the vegetation colonization taking ~17 years to start and following the primary succession dynamics. Our data confirm the importance of the ingress of pioneer species typical of scree slopes for the initial stages of succession (*Androsacetum alpinae*).[60]

The ski-run area is an anthropogenic surface but, given its elevation, the type of substrata (reworked morainic deposits) and the lack of recovery actions, we could compare our data with the patterns and rates of vegetation colonization of glacier forefields provided in the literature and available especially for the European Alps. In the alpine belt the colonization of recently deglaciated terrains is reported to start within 4–8 years after deglaciation,[63–65] with scattered early-successional pioneer species. At least 10–25 years are required for the ingress of early-successional species (with the development of the *Oxyrietum digynae*) and the development of a well-established early-successional community (e.g. *Luzuletum spadiceae*).[65–69] In many cases

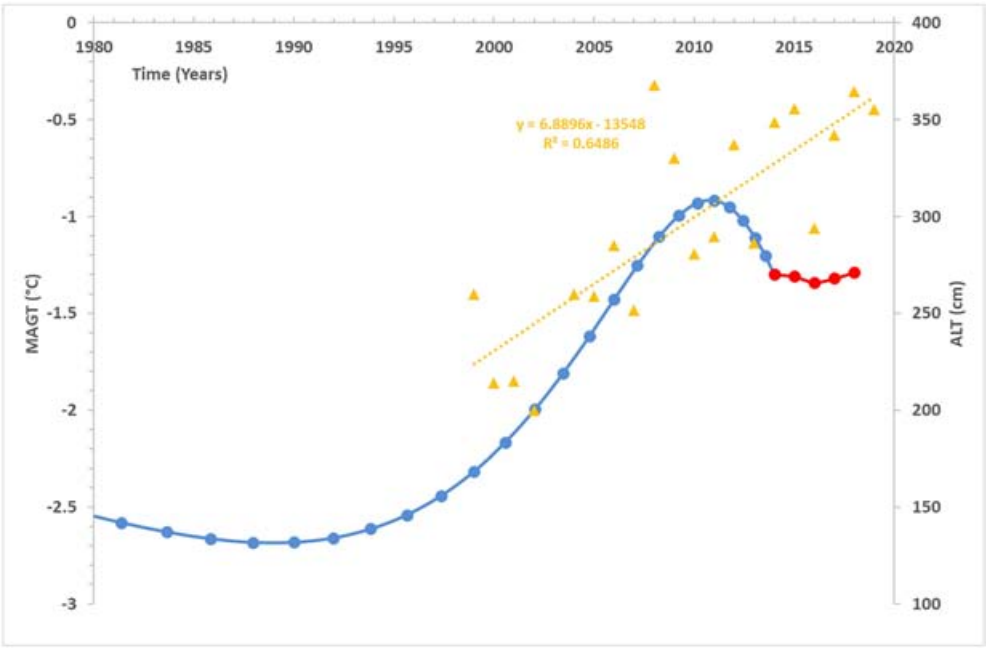

FIGURE 13 Permafrost temperature and ALT variations at the SSB site (see Figure 1) located at 3,000 m asl. The blue line indicates the reconstruction of the mean annual permafrost temperature according to Guglielmin et al.,[25] and the red line indicates the mean annual permafrost temperature at the DZAA recorded in the borehole in the last 5 years. Orange triangles are the ALT values since 1998 at the same site, and the dashed orange line is its linear regression

the vegetation succession on glacier forefields may take more than a century, involving waves of immigration, where pioneer species are replaced by snowbed or heath species, with concomitant decreases in soil moisture, and increases in nutrient availability as soil pH values fall (e.g., [70,71]).

Cannone et al.[46] reported that in the early 2000s, at a site relatively close to our study area and located at a comparable elevation (Sforzellina glacier), the vegetation colonization of recently deglaciated surfaces exhibited a dramatic acceleration in response to climate warming. The first plant species colonized the glacier forefield only 1 year after glacier retreat, and showed a prevalence of scree slope instead of snowbed species.

Our data show that the colonization of the ski run was very slow until the early 2000s, requiring more than double the time taken to colonize recently deglaciated glacier forefields (17 vs 8–10 years) for the first ingress of plants. This initial delay confirms the harshness of the ski-run environment. This could be due to the particular conditions of the ski run, characterized by substantial alterations of soils with a relatively hard surface of compacted material (not allowing the permanence of seeds and the fixing of the new plantulae to the terrain), the lack of nutrients, and high pH (e.g., [60–62]). Moreover, the ski run is characterized by the lack of a soil with a seed bank, which may increase substantially the speed of vegetation colonization, as observed in the colonization of landslides in periglacial environments (e.g., [72]).

After this first stage of colonization started in the early 2000s, at the same time as the documented onset of thermokarst activity, the vegetation succession developed rapidly. Rates of succession were similar to those described by Cannone et al.,[46] much faster than those reported in literature for the "normal" succession of glacier forefields and also much faster than the rates of spontaneous revegetation of ski runs, especially at high elevation (e.g., [60–62]). The patterns of vegetation succession indicated that species were recruited mainly from the surrounding areas, with contributions from both the pioneer and snowbeds communities. Similar recruitment has been shown by Cannone and Pignatti[38] when analyzing the effects of climate warming on the composition of alpine plant communities, and unravelling the role of range filling of communities within a belt instead of processes of long-term upslope migration. We show that the main recruitment sources are neighboring communities within the same elevation belt, performing biotic exchanges with other plant communities in the same altitudinal belts.

We also show that thermokarst depressions are characterized by slower vegetation dynamics, as both the successional stages and the species richness are less developed than the remaining ski run. This could be due to the greater surface disturbance within the depressions linked to their dynamics, as it is known that only some selected plant species (such as *Cerastium uniflorum*) are able to colonize and persist on such terrain (e.g., [73–75]). Our data confirm the importance of surface disturbance due to periglacial and paraglacial processes within the depressions in affecting the patterns of vegetation succession, as observed for glacier forefields and/or periglacial features (e.g., [70,71]). Indeed, the steep slopes where thermokarst features develop may increase surface instability, expressed by geomorphic processes such as nivation, solifluction and interactions between them.[75] Another factor that could inhibit vegetation development is the documented longer permanence of snow cover inside the depressions, decreasing substantially the length of the growing season and providing a further selection of chionophilous species able to adapt to these harsh conditions (such as *Arenaria biflora*, *Veronica alpina*, *Gnaphalium supinum*). The importance of snow cover persistence is also confirmed by the occurrence of moss patches at the bottom of the deepest depressions.

It is notable that the occurrence of subalpine shrub species belonging to the genus *Salix* confirms the further acceleration of the succession dynamics (as it started less than 20 years after construction of the ski-run and was a spontaneous process). This indicates that an important ecological change is occurring in the study area, probably in response to climate and environmental change. Indeed, according to the existing literature, the ingress of shrubs may occur only after several decades, as observed both for glacier forefields and for restored ski runs. However, the colonization by *Salix* shrubs just stops close to the thermokarst area and involves only the part of the ski run located at lower elevation than the thermokarst depressions.

6 | CONCLUSIONS

This study has documented for the first time, to the best of our knowledge, the development of thermokarst depressions on an anthropogenic surface at high elevation in mid-latitude mountains. These landforms developed during a phase of permafrost degradation that started after 2002, when the mean annual permafrost temperature at the DZAA in the adjacent SSB was around −2°C. The thermokarst depressions formed without any lake, probably due to the coarse grain size and probably high hydraulic conductivity of the host deposits, the steepness of the slope (only for depressions 3 and 4), and the limited ice content in the artificial material used for the ski-run construction. At the same time, the vegetation changed rapidly during permafrost degradation and culminated with the arrival of some subalpine shrub species belonging to the genus *Salix*. Their arrival indicates that an important ecological change is occurring in the whole study area, as also testified by the repeated geophysical measurements, which show accelerated vegetation dynamics in response to accelerated climate change.

All these observed features show a rapid and coupled response of both the abiotic and the biotic components of ecosystems to climate warming, with an acceleration of the impacts on the environment. Our data also confirm the similarity between the observed responses and dynamics of the alpine tundra with the Arctic tundra concerning the evolution of both permafrost and vegetation.

ORCID

Mauro Guglielmin https://orcid.org/0000-0002-5966-9572

REFERENCES

1. French HM. *The Periglacial Environment*. Fourth ed. Chichester, UK: Wiley and Sons; 2017.
2. Washburn AL. *Geocryology: A survey of Periglacial Processes and Environments*. London, UK: Edward Arnold; 1979.
3. Van Everdingen RO. Multi-language Glossary of Permafrost and Related Ground-ice Terms. International Permafrost Association, University of Calgary, USA: 1998.
4. Jorgenson MY, Shur YL, Osterkamp TE. Thermokarst in Alaska. In: Kane DL, Hinkel KM, eds. *Proceedings of the Ninth International Conference on Permafrost, 29 June – 3 July 2008, Fairbanks, Alaska*. Fairbanks, Alaska: Institute of Northern Engineering, University of Alaska Fairbanks; 2008:869-876.
5. Farquharson LM, Romanovsky VE, Cable WL, Walker DA, Kokelj SV, Nicolsky D. Climate change drives widespread and rapid thermokarst development in very cold permafrost in the Canadian high Arctic. *Geophys Res Lett*. 2019;46(12):6681-6689.
6. Lewkowicz AG, Way RG. Extremes of summer climate trigger thousands of thermokarst landslides in a high Arctic environment. *Nat Commun*. 2019;10(1):1329.
7. Jorgenson MT. Thermokarst terrains. In: Shroder J, Giardino R, Harbor J, eds. *Treatise in Geomorphology, 8, glacial and periglacial geomorphology*. San Diego: Academic Press; 2013:313-324.
8. Kokelj SV, Jorgenson MT. Advances in thermokarst research. *Permafrost Periglac Process*. 2013;24(2):108-119.
9. Soare RJ, Conway SJ, Williams JP, Gallagher C, McKeown LE. Possible (closed system) pingo and ice-wedge/thermokarst complexes at the mid latitudes of utopia Planitia, Mars. *Icarus*. 2020;342:113233.
10. Bodin X, Brenning A, Rojas F. Status and evolution of the cryosphere in the Andes of Santiago (Chile, 33.5° S). *Geomorphology*. 2010;118 (3-4):453-464.
11. Monnier S, Kinnard C. Pluri-decadal (1955-2014) evolution of glacier-rock glacier transitional landforms in the Central Andes of Chile (30-33° S). *Earth Surf Dyn*. 2017;5(3):493-509.
12. Kääb A, Haeberli W. Evolution of a high-mountain thermokarst lake in the Swiss Alps. *Arct Antarct Alp Res*. 2001;33(4):385-390.
13. Haeberli W, Kääb A, Mühll DV, Teysseire P. Prevention of outburst floods from periglacial lakes at Grubengletscher, Valais, Swiss Alps. *J Glaciol*. 2001;47(156):111-122.
14. Romanovsky VE, Smith SL, Christiansen HH. Permafrost thermal state in the polar northern hemisphere during the international polar year 2007–2009: a synthesis. *Permafrost Periglac Process*. 2010;21(2): 106-116.
15. Biskaborn BK, Smith SL, Noetzli J, et al. Permafrost is warming at a global scale. *Nat Commun*. 2019;10(1):264.
16. Godin E, Fortier D, Coulombe S. Effects of thermo-erosion gullying on hydrologic flow networks, discharge and soil loss. *Environ Res Lett*. 2014;9(10):105010.
17. Liljedahl AK, Boike J, Daanen RP, et al. Pan-Arctic ice-wedge degradation inwarming permafrost and its influence on tundra hydrology. *Nat Geosci*. 2016;9(4):312-318.
18. Wrona FJ, Johansson M, Culp JM, et al. Transitions in Arctic ecosystems: ecological implications of a changing hydrological regime. *J Geophys Res-Biogeo*. 2016;121(3):650-674.
19. Rudy ACA, Lamoureux SF, Kokelj SV, Smith IR, England JH. Accelerating thermokarst transforms ice-cored terrain triggering a downstream cascade to the ocean. *Geophys Res Lett*. 2017;44(21):11-080.
20. Perreault N, Lévesque E, Fortier D, Gratton D, Lamarque LJ. Remote sensing evaluation of high Arctic wetland depletion following permafrost disturbance by thermo-erosion gullying processes. *Arctic Sci*. 2017;3(2):237-253.
21. Nelson FE, Anisimov OA, Shiklomanov NI. Climate change and hazard zonation in the circum-arctic permafrost regions. *Nat Hazards*. 2002; 26(3):203-225.
22. Doré G, Niu F, Brooks H. Adaptation methods for transportation infrastructure built on degrading permafrost. *Permafrost Periglac Process*. 2016;27(4):352-364.
23. De Pascale GP, Pollard WH, Williams KK. Geophysical mapping of ground ice using a combination of capacitive coupled resistivity and ground-penetrating radar, Northwest Territories, Canada. *J Geophys Res-Earth*. 2008;113:F02S90.
24. Short N, LeBlanc AM, Sladen W, Oldenborger G, Mathon-Dufour V, Brisco B. Radarsat-2 D-InSAR for ground displacement in permafrost terrain, validation from Iqaluit airport, Baffin Island, Canada. *Remote Sens Environ*. 2014;141:40-51.
25. Guglielmin M, Tellini C. Contributo alla conoscenza Dei rock glaciers delle Alpi italiane. I rock glaciers del Livignasco (Alta Valtellina). *Riv Geogr Ital*. 1992;99:395-414.

26. Montrasio A, Berra F, Cariboni M, et al. NOTE ILLUSTRATIVE della CARTA GEOLOGICA D'ITALIA alla scala 1:50.000. ISPRA (Istituto Superiore per la Protezione e la Ricerca Ambientale), SERVIZIO GEOLOGICO D'ITALIA, Organo cartografico dello Stato (legge 68 del 2-2-1960). 1990.
27. Guglielmin M. Permafrost e morfodinamica periglaciale nelle Alpi Centrali Italiane. Metodologie per l'individuazione del permafrost e dei processi e forme ad esso correlate [PhD Thesis]. Parma: Università di Parma; 1994.
28. Cannone N, Guglielmin M, Hauck C, Mühll DV. The impact of recent glacier fluctuation and human activities on permafrost distribution, Stelvio pass (Italian central-eastern Alps). *ICOP*. 2003;1:125-130.
29. Guglielmin M, Donatelli M, Semplice M, Capizzano SS. Ground surface temperature reconstruction for the last 500 years obtained from permafrost temperatures observed in the SHARE STELVIO borehole, Italian Alps. *Clim Past*. 2018;14(6):709-724.
30. Longhi A, Monticelli D, Guglielmin M. Iron chemical analysis of Podzols to date last Pleistocene-Holocene. The example of the Italian Central Alps. *J Quat Sci*. 2020;35(8):1021-1035.
31. Pelfini M. *Le fluttuazioni glaciali oloceniche nel gruppo Ortles-Cevedale (settore lombardo)* [PhD thesis]. Milano: Università degli Studi di Milano; 1992.
32. Ceriani M, Carelli M. Carta delle precipitazioni medie, minime e massime annue del territorio alpino lombardo (registrate nel periodo 1891-1990). Regione Lombardia-Direzione Generale Territorio Ed Edilizia Residenziale. 1999.
33. Guglielmin M, Siletto GB. *Carta della Criosfera*. Regione Lombardia: Direzione Generale Territorio ed Edilizia Residenziale; 2000.
34. Guglielmin M, Cannone N, Dramis F. Permafrost-glacial evolution during the Holocene in the Italian Central Alps. *Permafrost Periglac Process*. 2001;12(1):111-124.
35. Guglielmin M. Observations on permafrost ground thermal regimes from Antarctica and the Italian Alps, and their relevance to global climate change. *Global Planet Change*. 2004;40:159-167.
36. Boeckli L, Brenning A, Gruber S, Noetzli J. Permafrost distribution in the European Alps: calculation and evaluation of an index map and summary statistics. *Cryosphere*. 2012;6(4):807-820.
37. Cannone N, Sgorbati S, Guglielmin M. Unexpected impacts of climate change on alpine vegetation. *Front Ecol Environ*. 2007;5(7):360-364.
38. Cannone N, Pignatti S. Ecological responses of plant species and communities to climate warming: upward shift or range filling processes? *Clim Change*. 2014;123(2):201-214.
39. Giacomini V, Pignatti S. Flora e vegetazione dell'Alta Valle del Braulio con speciale riferimento ai pascoli di altitudine. *Mem Della Soc Ital di Sci Nat*. 1955;11:1-194.
40. Malfasi F, Cannone N. Climate warming persistence triggered tree ingression after shrub encroachment in a high Alpine tundra. *Ecosystems*. 2020;23:1657-1675.
41. Loke MH, Chamber JE, Rucker DF, Kuras O, Wilkinson PB. Recent development in the direct-current geoelectrical imaging method. *J Appl Geophys*. 2013;95:135-156.
42. Loke MH, Dahlin T. A comparison of gauss-Newton and quasi-Newton methods in resistivity imaging inversion. *J Appl Geophys*. 2002;49(3):149-162.
43. Kneisel C, Hauck C. Electrical methods. In: Hauck C, Kneisel C, eds. *Applied geophysics in periglacial environments*. Cambridge, UK: Cambridge University Press; 2008:3-27.
44. Jol HM (Ed). *Ground Penetrating radar: theory and applications*. the Netherlands: Elsevier science; 2009.
45. Hofierka J, Gallay M, Bandura P, Šašak J. Identification of karst sinkholes in a forested karst landscape using airborne laser scanning data and water flow analysis. *Geomorphology*. 2018;308:265-277.
46. Cannone N, Diolaiuti G, Guglielmin M, Smiraglia C. Accelerating climate change impacts on alpine glacier forefield ecosystems in the European Alps. *Ecol Appl*. 2008;18(3):637-648.
47. Cannone N, Seppelt RD. A preliminary floristic classification of northern and southern Victoria land vegetation (continental Antarctica). *Antarct Sci*. 2008;20(6):553-562.
48. Favero-Longo SE, Worland MR, Convey P, et al. Primary succession of lichen and bryophyte communities following glacial recession on Signy Island, South Orkney Islands, maritime Antarctic. *Antarct Sci*. 2012;24(4):323-336.
49. Ellenberg H. *Vegetation ecology of Central Europe*. Cambridge, UK: Cambridge University Press; 1988.
50. Blasi C, Biondi E. *La flora in Italia*; Ministero dell'Ambiente e della Tutela del Territorio e del Mare. 2017.
51. ter Braak CJF, Šmilauer S. CANOCO reference manual and CanoDraw for windows user's guide: software for canonical community ordination (version 4.5). Ithaca, NY, microcomputer power, 500 pp. 2002.
52. Pignatti S. *La flora d'Italia*. Italia: Edagricole; 1982.
53. Lauber K, Wagner G. *Flora helvetica*. Berne (Switzerland): Verlag Paul Hapt Ed; 1998.
54. Conti F, Abbate G, Alessandrini A, Blasi C, Bonacquisti S, Scassellati E. An annotated checklist of the Italian vascular flora: first data. *Bocconea*. 2007;21:147-153.
55. Wilhalm T, Niklfeld H, Gutermann W. *Katalog der Gefäßpflanzen Südtirols.–Veröffentlichungen des Naturmuseums Südtirol*. Folio Verlag, Wien/Bozen und Naturmuseum Südtirol. *Hacquetia*. 2006;6(1): 1-215.
56. Uysal M, Toprak AS, Polat N. DEM generation with UAV photogrammetry and accuracy analysis in Sahitler hill. *Measurement*. 2015;73: 539-543.
57. Reuter HI, Hengl T, Gessler P, Soille P. Preparation of DEMs for geomorphometric analysis. *Dev Soil Sci*. 2009;33:87-120.
58. Masoud AA, Koike K. Tectonic architecture through LANDSAT-7 ETM+/SRTM DEM-derived lineaments and relationship to the hydrogeologic setting in Siwa region, NW Egypt. *J African Earth Sci*. 2006;45(4–5):467-477.
59. Etzelmüller B, Guglielmin M, Hauck C, et al. Twenty years of European mountain permafrost dynamics – the PACE legacy. *Environ Res Lett*. 2020;15(10):104070.
60. Wipf S, Rixen C, Fischer M, Schmid B, Stoeckli V. Effects of ski piste preparation on alpine vegetation. *J Appl Ecol*. 2005;42(2):306-316.
61. Barni E, Freppaz M, Siniscalco C. Interactions between vegetation, roots, and soil stability in restored high-altitude ski runs in the Alps. *Arct Antarct Alp Res*. 2007;39(1):25-33.
62. Hudek C, Barni E, Stanchi S, D'Amico M, Pintaldi E, Freppaz M. Mid and longterm ecological impacts of ski run construction on alpine ecosystems. *Sci Rep*. 2020;10(1):11654.
63. Stöcklin J, Bäumler E. Seed rain, seedling establishment and clonal growth strategies on a glacier foreland. *J Veg Sci*. 1996;7(1):45-56.
64. Burga CA. Vegetation development on the glacier forefield Morteratsch (Switzerland). *Appl Veg Sci*. 1999;2(1):17-24.
65. Tscherko D, Hammesfahr U, Zeltner G, Kandeler E, Böcker R. Plant succession and rhizosphere microbial communities in a recently deglaciated alpine terrain. *Basic Appl Ecol*. 2005;6(4): 367-383.
66. Pirola A, Credaro V. Changes in the vegetation of a recent glacial moraine in the Bernina group. *Ann Bot*. 1993;51:145-153.
67. Niederfriniger Schlag R, Erschbamer B. Germination and establishment of seedlings on a glacier foreland in the Central Alps, Austria. *Arc Antarct Alp Res*. 2000;32(3):270-277.
68. Caccianiga M, Andreis C. Pioneer herbaceous vegetation on glacier forefields in the Italian Alps. *Phytocoenologia*. 2004;34(1):55-89.
69. Raffl C. ErschbamerB. Comparative vegetation analyses of two transects crossing a characteristic glacier valley in the Central Alps. *Phytocoenologia*. 2004;32:225-240.
70. Haugland JE, Beatty SW. Vegetation establishment, succession and microsite frost disturbance on glacier forelands within patterned ground chronosequences. *J Biogeogr*. 2005;32:145-153.

71. Eichel J, Krautblatter M, Schmidtlein S, Dikau R. Biogeomorphic interactions in the Turtmann glacier forefield, Switzerland. *Geomorphology*. 2013;201:98-110.
72. Cannone N, Lewkowicz AG, Guglielmin M. Vegetation colonization of permafrost-related landslides, Ellesmere Island, Canadian high arctic. *J Geophys Res-Biogeo*. 2010;115(G4):G04020.
73. Cannone N, Gerdol R. Vegetation as an ecological indicator of surface instability in rock glaciers. *Arct Antarct Alp Res*. 2003;35(3):384-390.
74. Cannone N, Guglielmin M, Gerdol R. Relationships between vegetation patterns and periglacial landforms in northwestern Svalbard. *Polar Biol*. 2004;27:562-571.
75. Ponti S, Cannone N, Guglielmin M. A new simple topo-climatic model to predict surface displacement in paraglacial and periglacial mountains of the European Alps: the importance of ground heating index and floristic components as ecological indicators. *Ecol Indic*. 2021;120:106889. https://doi.org/10.1016/j.ecolind.2020.106889

How to cite this article: Guglielmin M, Ponti S, Forte E, Cannone N. Recent thermokarst evolution in the Italian Central Alps. *Permafrost and Periglac Process*. 2021;1–19. https://doi.org/10.1002/ppp.2099